Geochimica et Cosmochimica Acta 374 (2024) 72–84

Contents lists available at ScienceDirect

Geochimica et Cosmochimica Acta

journal homepage: www.elsevier.com/locate/gca

Aluminium substitution affects jarosite transformation to iron oxyhydroxides in the presence of aqueous Fe(II)

Andrew R.C. Grigg [a,*], Luiza Notini [a], Ralf Kaegi [b], Laurel K. ThomasArrigo [a,c], Ruben Kretzschmar [a]

[a] Soil Chemistry Group, Institute of Biogeochemistry and Pollutant Dynamics, Department of Environmental Systems Science, ETH Zurich, Universitätstrasse 16, CHN, CH-8092 Zurich, Switzerland
[b] Eawag, Swiss Federal Institute of Aquatic Science and Technology, Überlandstrasse 133, CH-8600 Dübendorf, Switzerland
[c] Environmental Chemistry Group, Institute of Chemistry, Avenue de Bellevaux 51, University of Neuchâtel, CH-2000 Neuchâtel, Switzerland

ARTICLE INFO

Associate editor: Juan Liu

Keywords:
Aluminium
Acid sulfate
Mineral(s)
Mössbauer spectroscopy
Iron isotopes

ABSTRACT

Jarosite is an abundant mineral in acidic environments, often found in acid sulfate soil (ASS) and acid-mine drainage (AMD). As a store of Fe, K, S and acidity, and a scavenger for major and trace elements, jarosite plays an important role in the biogeochemistry of acid sulfate environments. When ASS and AMD become anoxic, reducing conditions can set in, producing conditions that are outside the thermodynamic stability field of jarosite. In this study, we investigated the transformation of synthetic and natural jarosite with various degrees of Al-for-Fe substitution under circumneutral anoxic conditions in the presence of Fe(II), to understand the rates and pathways of jarosite and Al-jarosite transformation, the role of competing transformation pathways, the fate of Al during transformation and the different reactivity of natural and synthetic Al-jarosite. Synthetic jarosite (containing 0 %–7 % Al-for-Fe substitution) and a natural Al-substituted jarosite sample from an ASS in Thailand were suspended in solutions of ^{57}Fe(II) at pH 7 for 24 h under anoxic conditions. The chosen experimental conditions mimic the Fe(II) concentrations and pH found in flooded ASS under reducing conditions. Changes in mineral composition of the suspensions were determined by Rietveld analysis of X-ray diffraction patterns at six time points. The fate of Al was determined by XRD, Raman spectroscopy and energy dispersive X-ray spectroscopy analysis of the jarosite and product minerals. Different transformation pathways that occurred simultaneously were traced by using ^{57}Fe Mössbauer spectroscopy and aqueous Fe isotope composition. The analysis showed that 7 % Al-for-Fe substitution in jarosite more than halved the mineral transformation rate compared to unsubstituted jarosite, regardless of the Fe(II) concentrations. Indeed, 7 % Al-for-Fe substitution had a greater effect on the transformation rate than an order-of-magnitude decrease in the Fe(II) concentrations in all Al-for-Fe substitution treatments. The transformation products in all samples were goethite, lepidocrocite and ferrihydrite, with minor amounts of magnetite forming from jarosite with no or low Al-for-Fe substitution reacted with high Fe(II) concentrations. Lepidocrocite was the dominant product in reactors without aluminium, but lepidocrocite was not strongly enriched in ^{57}Fe, suggesting that it may not have formed exclusively from Fe in solution during the Fe(II)-catalysed transformation of other minerals. In high-Al systems, lepidocrocite appeared to be a sink for Al, although its formation in Al-rich samples was suppressed. Natural jarosite reacted more than an order of magnitude more slowly than the synthetic jarosite and Al-jarosite, indicating that the properties of the synthetic jarosite do not completely account for the stability of natural jarosite under anoxic circumneutral conditions. The results provide an important baseline for understanding the drivers of jarosite transformation or stability in ASS and AMD.

1. Introduction

Jarosite is a potassium-iron hydroxysulfate mineral that is commonly formed in acidic, sulfur- and oxygen-rich environments. Jarosite has the general formula $AB_3(TO_4)_2(OH)_6$ (Menchetti and Sabelli, 1976), where the B site contains mostly Fe^{3+}. As a member of the alunite supergroup

* Corresponding author.
E-mail address: andrew.grigg@usys.ethz.ch (A.R.C. Grigg).

https://doi.org/10.1016/j.gca.2024.04.008
Received 27 October 2023; Accepted 5 April 2024
Available online 7 April 2024

of minerals, Al is the most important substituent at the B site in jarosite and a complete solid solution series exists between jarosite and alunite (B site completely occupied by Al) according to Vegard's law (Jones, 2017). The A site is most commonly occupied by K^+, Na^+, H_3O^+ or NH_4^+, but may also contain Ag^+, Ba^{2+}, Bi^{3+}, Ca^{2+}, Pb^{2+}, Rb^+, Sr^+, Tl^+, Th^{4+}, rare earth elements (REE) and others (Stoffregen et al., 2000; Welch et al., 2007). The T site is mostly occupied by S^{6+}, but also commonly contains P^{5+} or As^{5+} (Stoffregen et al., 2000). As a prominent product of sulfuricisation (by sulfate reduction; Fanning, 1993), jarosite may be diagnostic of oxidation processes occurring in acid sulfate soil (ASS), acid mine drainage (AMD) and supergene pyrite deposits (Bigham and Nordstrom, 2000). The occurrence of jarosite in other niche environments, such as hypersaline lakes (Alpers et al., 1992), Antarctic ice (Baccolo et al., 2021), and the surface of Mars (Klingelhöfer et al., 2004), provides important information about the (geo)chemical history of those environments. In hydrometallurgical industries, jarosite precipitation is induced to remove undesirable impurities (Dutrizac and Jambor, 2000).

In ASS and AMD, jarosite affects the mobility of Fe, S and other major and trace elements, as well as the release of acidity. The stability of jarosite may be critical to the immobilisation of toxic elements that are incorporated into the jarosite structure, or sorbed to its surface, as these elements may be mobilised during jarosite transformation and dissolution (Karimian et al., 2017, 2018; Ryu and Kim, 2022; Welch et al., 2007). Structural jarosite incorporation of trace elements such as As, Cr, Mo and Se (Kendall et al., 2013; Ryu and Kim, 2022), and sorption of Si and organic compounds (Jones et al., 2009), have also been shown to alter the rates and pathways of jarosite transformation. Although strong links have been demonstrated between jarosite and the biogeochemical cycling of numerous elements in soils, the effect of Al on jarosite stability and the effect of jarosite on Al mobility are poorly understood in environmental systems. Concentrations of Al in pore waters of ASS in Thailand and Malaysia have been recorded up to 2.12 mM (Van Breemen, 1973) and as much as 23 % of readily available Al in an Australian ASS was associated with Fe minerals (Yvanes-Giuliani et al., 2014). Recently, jarosite that was isolated from ASS in Thailand was shown to have at least 5 % Al-for-Fe substitution (Grigg et al., 2024), mirroring observations of Al-for-Fe substitution in jarosite from other natural environments (Alpers et al., 1992; Johnston, 1977; Sánchez-España et al., 2016) and in hydrometallurgical waste (Pappu et al., 2006). Since Al is one of the primary causes of toxicity to plants and aquatic life in acid sulfate systems (Ljung et al., 2009; Powell and Martens, 2005; Van Breemen, 1973), the controls on its mobility need to be understood. Moreover, Al substitution alters the structural properties of jarosite (Grigg et al., 2024), which may affect rates and pathways of jarosite transformation in soils.

Jarosite reactivity has been measured in laboratory mixed-suspension systems that simulate various aspects of dynamic acid sulfate environments. Under oxic conditions, jarosite transformation occurs over the course of several months in solutions with pH between 2 and 8 (Smith et al., 2006; Welch et al., 2008). Faster transformation occurs under anoxic conditions in the presence of Fe(II) (Jones et al., 2009; Karimian et al., 2017, 2018). For example, a study of jarosite in an anoxic solution at pH 6.5 (buffered with 2-(N-morpholino)ethanesulfonic acid, commonly known as 'MES') and containing a ratio of Fe (II)-spike to mineral-Fe(III) (henceforth called 'Fe(II)-to-Fe(III) ratio') of 0.4 showed complete transformation within fewer than 7 days to 73.5 % lepidocrocite and 26.5 % ferrihydrite (Jones et al., 2009). The transformation was inhibited in the presence of Si and organic matter (Jones et al., 2009). Another study of synthetic As- and Sb-bearing jarosite transformation with Fe(II)-to-Fe(III) ratios between 0.045 and 0.9 in a solution at pH 7.0 (buffered with MES and 3-(N-morpholino)propanesulfonic acid, commonly known as 'MOPS') showed rapid (<24h) transformation to green rust, lepidocrocite and goethite in varying ratios (Karimian et al., 2017). Increasing acidity slows the rate of Fe(II)-catalysed jarosite transformation (Karimian et al., 2018; Whitworth et al., 2020). At pH 5.5, with Fe(II)-to-Fe(III) ratio of 0.9, partial jarosite transformation to goethite was observed after 24 h, and at pH 4 no transformation occurred within 24 h (Karimian et al., 2018). Moreover, at pH <4.5, in the presence of 0.25 mM Fe(II) and 10 mM Na_2SO_4, transformation of jarosite (2000 mg/L) was not observed in 70 days, although up to 1.82 % of the atoms in the jarosite and Na-jarosite were exchanged by Fe(II)-catalysed stable mineral recrystallisation (Whitworth et al., 2020). Together, these studies reveal several processes that result in jarosite transformation, with the dominance of each being dependent on the chemical composition of the suspension, including pH and Fe(II) concentration, and element substitution in jarosite.

Building on previous studies of jarosite stability, we sought to deconvolve the competing processes that cause jarosite transformation under circumneutral anoxic conditions and consider the effect of cation substitution (specifically Al-for-Fe substitution) on the Fe(II)-catalysed transformation of jarosite. Therefore, the objectives of our study were to assess four novel aspects of the transformation of jarosite under anoxic circumneutral conditions: (1) the effect of Fe and Al occupancy on the stability and transformation pathways of jarosite-alunite group minerals, (2) the fate of Al during the transformation of Al-jarosite, (3) the relative dominance of competing pathways of jarosite transformation, and (4) the difference in reactivity between synthetic and natural jarosite. To achieve this, samples of synthetic jarosite, synthetic Al-jarosite and natural jarosite were reacted with ^{57}Fe(II) at pH 7.1 in mixed-suspension batch experiments for twenty-four hours. The Fe(II) concentration and circumneutral conditions in the reaction solution were designed to mimic the Fe(II):Fe(III) ratios and pH typically found in the porewater of some flooded acid sulfate topsoil under reducing conditions (Burton et al., 2011; Karimian et al., 2017; Kölbl et al., 2017). The transformation processes were observed by quantifying the changes in the mineralogy and solution chemistry in the reactors over the course of the experiments.

2. Methods

2.1. Mineral synthesis and collection of natural jarosite

Synthetic jarosite minerals with varying Al contents were synthesised by a hydrothermal method (Driscoll and Leinz, 2005) that is described in detail in Grigg et al. (2024). In brief, solutions of 0.9 M Fe (III) were prepared by dissolution of Fe(0) (10 μm metal powder, EMSURE analysis grade, Merck) in 2 M H_2SO_4 (95–95 % reagent grade, Sigma Aldrich) followed by oxidation with excess H_2O_2 (35 %, Merck). The Fe(III) solutions were mixed in appropriate ratios with a saturated solution of $AlK(SO_4)_2{\cdot}12H_2O$ (Normapur reagent grade, VWR), to produce solutions with Al/(Fe+Al) = 0 (from which unsubstituted jarosite was synthesised), Al/(Fe+Al) = 0.05 (which produced 1 % Al-for-Fe substitution in the synthesised jarosite, henceforth referred to as low-Al jarosite) and Fe/(Fe+Al) = 0.3 (which produced 7 % Al-for-Fe substitution in the synthesised jarosite, henceforth referred to as high-Al jarosite). Solutions were adjusted to pH 2.5 ± 0.05 with KOH (pellets extra pure, Merck) and heated to 140 °C for 5h. The precipitates were rinsed with ultra-pure water (UPW; MilliQ, Millipore, >18.2 MΩ·cm), oven dried for 24 h at 60 °C, gently homogenised with a mortar and pestle and stored in amber glass vials in a desiccator. The natural jarosite used in this study was collected from jarosite nodules (regions of soil that are highly enriched in jarosite) found between 68 and 135 cm depth in an ASS profile in Chachoengsao province, Thailand. The profile was sampled in February 2020 after the field had been drained for several months. The jarosite-bearing soil samples were dried at 30 °C, and jarosite was hand-picked using a scalpel. Elemental and structural analysis of the synthetic and natural jarosite used in this study are reported in Section S1 and Grigg et al. (2024).

2.2. Transformation experiment design

Jarosite transformation was investigated in triplicate mixed batch reactors containing a suspension of natural jarosite, or synthetic unsubstituted, low-Al or high-Al jarosite in an anoxic solution of 50 mM MOPS buffer (pH 7.1) and 0 mM, 0.5 mM or 5 mM ^{57}Fe(II) (henceforth referred to as no-Fe(II), low-Fe(II) and high-Fe(II) treatments, respectively). To set up the experiment, jarosite (85.6 mg, 86.6 mg, 91.9 mg and 101 mg per vial for unsubstituted, low-Al, high-Al and natural jarosite, respectively) was weighed into 100 mL glass septum bottles (henceforth 'reactors'). The jarosite solid-to-solution ratio was varied to ensure that each reactor contained the same Fe(II)-to-Fe(III) ratio. The Fe(III) content of jarosite varied because of substitution for Fe or deficiency at the B site (Grigg et al., 2024). The reactors were transferred to a glove box (MBRAUN; N_2 atmosphere, <1 ppm O_2) >48 h before the experiments began. The MOPS solution was added to each bottle one hour (t = −1 h) before the addition of a ^{57}Fe(II) spike (at t = 0). To produce the no-Fe(II), low-Fe(II) and high-Fe(II) treatments, 0 μL, 76 μL or 760 μL, respectively, of a concentrated ^{57}Fe solution was added, which was calculated to bring the final volume of each reactor to 90 mL. The concentrated ^{57}Fe(II) spike solution was produced by dissolution of ^{57}Fe(0) powder (Isoflex, USA; certified ^{57}Fe purity 96.14 %) in 2 M HCl (NORMATOM, VWR), which was then filtered with a nylon syringe filter to 0.22 μm and measured using inductively coupled plasma with optical emission spectroscopy (ICP-OES) to determine the final Fe concentration. Jarosite masses and spike concentrations were chosen to produce a ratio of 1:10 Fe(II):Fe(III) in low-Fe(II) treatments and 1:1 Fe(II):Fe(III) in high-Fe(II) treatments. The ratios are comparable to those used in previous jarosite transformation experiments (up to 1:0.9 (Karimian et al., 2017) and 1:2.5 (Jones et al., 2009)) and found in reflooded ASS wetland (1:1.1 ratio of aqueous Fe(II) in pore water to Fe(III) in dithionate-extractable phases (Burton et al., 2011; Karimian et al., 2017)). All reactors were capped with rubber stoppers, placed on an orbital shaker and protected from light during the experiment.

Each reactor was sampled at 0.5, 1, 2, 4, 8 and 24 h after the beginning of the experiment, except for no-Fe(II) reactors which were measured at 0, 1, 8 and 24 h. The high-Al high-Fe(II) reactors were sampled at 51 h instead of 24 h, and so a separate experiment was run to capture the 24-hour timepoint. Due to observably slower reaction kinetics, reactors containing natural jarosite were additionally sampled after 7 days. At each sampling timepoint, reactors were manually shaken to ensure homogeneous suspension of particles, then an aliquot of 10 mL was poured into an open 10 mL syringe and filtered through a 0.22 μm mixed cellulose ester (MCE) filter. After discarding the first millilitre of the filtered solution, 4 mL was preserved in 1 % HCl (Normatom, VWR) and stored at 4C until analysis. The solids were retained for later analysis with powder X-ray diffraction (XRD) and Raman spectroscopy. All solids were rinsed with UPW before being dried in the glove box atmosphere on the MCE filter. Once dry, the mineral samples were scraped off the filter paper and stored in the dark in the glove box. The triplicate solid samples from each timepoint were combined, except for 1-hour samples, for which individual replicates were measured to estimate variability. At the 1-hour timepoint, in addition to the 10 mL filtration for XRD and Raman spectroscopy analysis, an additional aliquot of approximately 45 mL per reaction vessel was filtered. The filtrate was discarded, but solids were rinsed, dried and combined, as described above, for Mössbauer spectroscopy and electron microscope (EM) analysis.

2.3. Analytical methods

Concentrations of Fe and S in filtered solutions were measured by ICP-OES (5100, Agilent Technologies, USA). Concentrations of K were measured by atomic absorption spectrometry (AAS, 240FS spectrometer, Agilent Technologies, USA) at 766.5 nm with sample atomisation in an air-acetylene flame. Isotopic ratios of Fe were measured by inductively coupled plasma mass spectrometry (ICP-MS, 8800 triple quad, Agilent Technologies, USA). Samples for isotope analysis were first measured for Fe concentration by ICP-OES, then diluted to 100 ppb Fe and measured by ICP-MS in reaction cell mode with an H_2 flow rate of 7 mL min^{-1}. Iron isotopic composition was reported as the counts of the ^{57}Fe divided by the sum of the counts of isotopes ^{54}Fe, ^{56}Fe, ^{57}Fe, and ^{58}Fe (Schulz et al., 2022).

Selected samples were examined by scanning transmission electron microscope (STEM, 2700Cs, Hitachi) and mapped by energy-dispersive X-ray (EDX) spectroscopy (FEI Talos F200X S/TEM microscope). Both analyses were carried out on the same samples, which were prepared by resuspension of approximately 2 mg of mineral in UPW and drop deposition onto 200-mesh Cu grids with holey carbon support film (SPI supplies, USA). Reacted mineral samples were prepared for STEM analysis in a glove box.

Powder XRD measurements from the transformation experiment were performed on dried solid samples that were resuspended in ethanol, transferred onto polished Si wafers (711 cut, Sil'tronix Silicon Technologies, France), allowed to dry in place and closed under anoxic seal. Samples were analysed in Bragg–Brentano geometry using Cu Kα radiation ($\lambda_{K\alpha1}$ = 1.540562 Å, $\lambda_{K\alpha2}$ = 1.544398 Å, 40 kV, 40 mA) and a high-resolution energy-dispersive 1D detector (D8 Advance, Bruker, USA; LYNXEYE detector). Measurements were taken between 10° and 70° 2θ with a step size of 0.02° 2θ and measurement time of 4 s/step. Rietveld quantitative phase analysis was performed on TOPAS software (Version 5, Bruker, USA), using previously published Crystallographic Information Files (CIF) for jarosite (Inorganic Crystal Structure Database, ICSD, no. 12107; Menchetti and Sabelli, 1976), goethite (ICSD no. 239321; Zepeda-Alarcon et al., 2014), lepidocrocite (ICSD no. 93948; Zhukhlistov, 2001) and magnetite (ICSD no. 26410; Fleet, 1981) and using a PONKCS (Scarlett and Madsen, 2006) phase calibration of synthetic ferrihydrite (Grigg et al., 2022), as described by ThomasArrigo et al. (2018). Calculations of mineral proportions, crystallite sizes and unit cell dimensions are based on Rietveld fits of full X-ray diffractograms except where the domain was explicitly restricted to particular peaks.

Raman spectroscopic analysis (inVia 2 confocal Raman microscope, Renishaw plc, UK) was performed following XRD analysis, using the same samples without anoxic seal. Measurements used a 532 nm laser (100 mW, Nd:YAG), 1800 l mm^{-1} grating and 50X objective with 0.5 % laser power and spot size of 1.3 μm. Sample spectra are the average of >1500 measurements taken for 8 s at different locations. Automatic focusing (LiveTrackTM focus tracking; Renishaw plc, 2018, Renishaw Technical Note no. TN214(EN)-01-A) was used to account for the rough surface.

Mössbauer spectroscopy was performed on samples that were made by combining approximately equal proportions of each triplicate collected at the 1-hour timepoint. Samples were dried and sealed in polyimide film tape (Kapton, 3M Company, USA) inside the glove box. Spectra were collected on a WSS-10 spectrometer (WissEL GmbH, Germany) in transmission using a ^{57}Co/Rh γ-radiation source. A liquid-He cryostat (Janis Research, USA) was used to cool samples to 4.2 K or 77 K throughout the measurements. Mössbauer spectral fitting employed extended Voigt-based fitting (xVBF), implemented in Recoil software (Lagarec and Rancourt, 1997; Rancourt and Ping, 1991). The Lorentzian full width half maximum was set to 0.135 mm/s for all fits. The velocity scale was calibrated to a measurement of α-Fe foil.

2.4. Modelling of ^{57}Fe distribution

Isotopes of Fe were used to trace the dominant mineral transformation pathways in the reactors. Initially, the Fe(II) in solution was enriched in ^{57}Fe, while the Fe(III) in jarosite had a natural isotope abundance, containing 2.12 % ^{57}Fe (Taylor et al., 1992). After the start of the experiment, any enrichment or depletion of ^{57}Fe in an Fe phase relative to the initial Fe isotope signature in the solid or solution could theoretically be caused by the flows of Fe atoms that occur during

mineral transformation. Whereas the isotopic composition of Fe mineral phases does not affect quantification by Rietveld fitting of XRD patterns, Mössbauer spectroscopy is only sensitive to the 57-isotope of Fe. In principle, the difference in the distribution of Fe between mineral phases as estimated by XRD and Mössbauer spectroscopy could be indicative of enrichment or depletion of ^{57}Fe in those phases. To interpret the processes that cause the enrichment or depletion of ^{57}Fe in mineral phases, a model was developed to calculate the rate of atom flow between defined Fe pools according to a conceptual model of the reaction space.

To implement the atom-flow model, total Fe and ^{57}Fe in the system were initially allocated to one of five pools — jarosite, ferrihydrite, goethite, lepidocrocite and dissolved/sorbed Fe — according to initial experimental conditions. Then, the pools were linked by a set of hypothetical transformation processes, which are described in Fig. 1. The total Fe and ^{57}Fe distribution in each pool was updated at discrete timesteps of 0.02 h by calculation of atom flows using guessed pseudo first-order rate constants (for justification see Section S7.1) for each hypothetical transformation pathway. Following each model run, the guessed rate constants were updated by a Monte-Carlo random walk procedure coupled to minimisation of the total sum of squares (SST). The SST was calculated at each of the six timesteps between predicted and measured solution Fe concentration, Fe isotopic composition in solution, and abundance of each of the four mineral phases considered. Iron concentration, Fe isotopic composition and mineral abundance were determined by ICP-OES, ICP-MS and XRD, respectively. Once the optimum set of rate constants was established, which minimised the SST, the isotopic composition of each Fe pool was calculated at the 1-hour timepoint. The plausibility of the atom flow model was validated by comparison of the expected ^{57}Fe distribution with ^{57}Fe measurements by ^{57}Fe Mössbauer spectroscopy and ICP-MS. For direct comparison, measured Mössbauer spectra were compared to reconstructed spectra that were calculated using the typical parameters for each Fe phase (Table S2) and the ^{57}Fe distribution that was predicted by the atom-flow model. The modelling procedure is illustrated in Fig. 1 and full details are provided in Section S7.

3. Results

3.1. Solution chemistry

The concentration of Fe, S, K and Al in solution were monitored throughout the experiment to observe the dynamics of the elements that constitute jarosite and Al-jarosite during its transformation. In addition, the isotopic composition of the Fe in solution was measured to monitor Fe exchange between the solution and the solids. Increases in the aluminium concentration in solution were not observed in no-Al, low-Al or high-Al reactors (Fig. S1), consistent with the low solubility of Al at circumneutral pH (Driscoll and Schecher, 1990). Increases in the solution S concentration were observed in all experiments, consistent with jarosite dissolution, but occurred on top of a high S background due to the S content of the MOPS buffer (Fig. S2). Changes in K concentration and Fe isotopic composition could be quantified using pseudo-first-order rate kinetic models, as described in Section S2.1 and S2.2, respectively (Fig. 2). The pseudo-first-order rate coefficients are reported in Table 1.

The Fe concentration in solution did not reflect the trend of mineral transformation or dissolution, as Fe was reincorporated into product phases. A rapid decrease in the solution Fe concentration occurred after the initial addition of Fe(II) (7–10 % in high-Fe(II) and 18–19 % in low-Fe(II) reactors with synthetic jarosite after two hours; Fig. S3), likely due to sorption of Fe(II) to mineral surfaces. The initial decrease in Fe concentration was slowest in suspensions of natural jarosite. Some further decreases after the initial rapid decrease in high-Al high-Fe(II) reactors occurred, likely due to the incorporation of Fe(II) into mixed-valent Fe mineral phases, such as magnetite. The ^{57}Fe composition of the solution approached a stable value equivalent to the total isotopic ratio of the reaction system (see calculation in Section S2.2). The stable value was reached at rates between 0.2 h^{-1} and 3.5 h^{-1} (natural jarosite with high-Fe(II) and unsubstituted low-Fe(II), respectively; Table 1).

The concentration of K increased throughout the transformation experiments, and approached a stable concentration within 24 h in reactors containing synthetic minerals and low- or high-Fe(II). In the hour before the addition of Fe(II), the solution K concentration reached 0.31 ± 0.06 mM in reactors containing unsubstituted jarosite and 0.39 ±

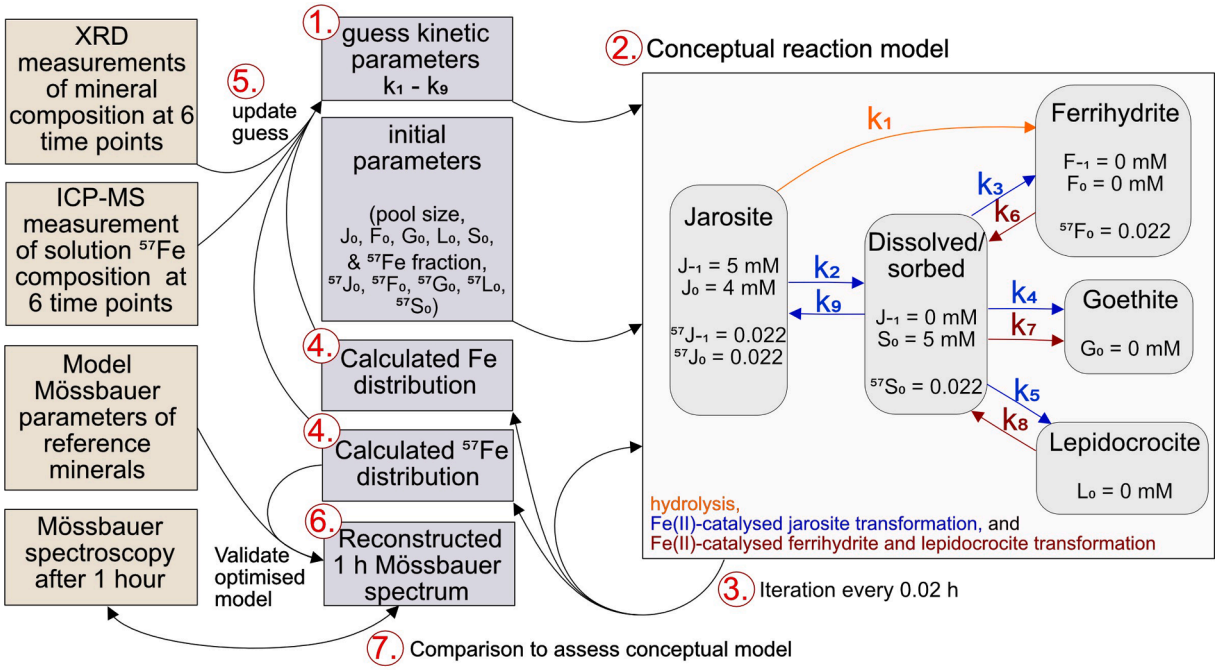

Fig. 1. Flow chart showing the conceptual model of Fe transfer between pools in the reactors and the framework used to integrate measured data into the modelling scheme. Red circled numbers indicate the order of processes in the modelling scheme. Note that the arrows within the conceptual reaction model indicate the direction of Fe atom flow between pools.

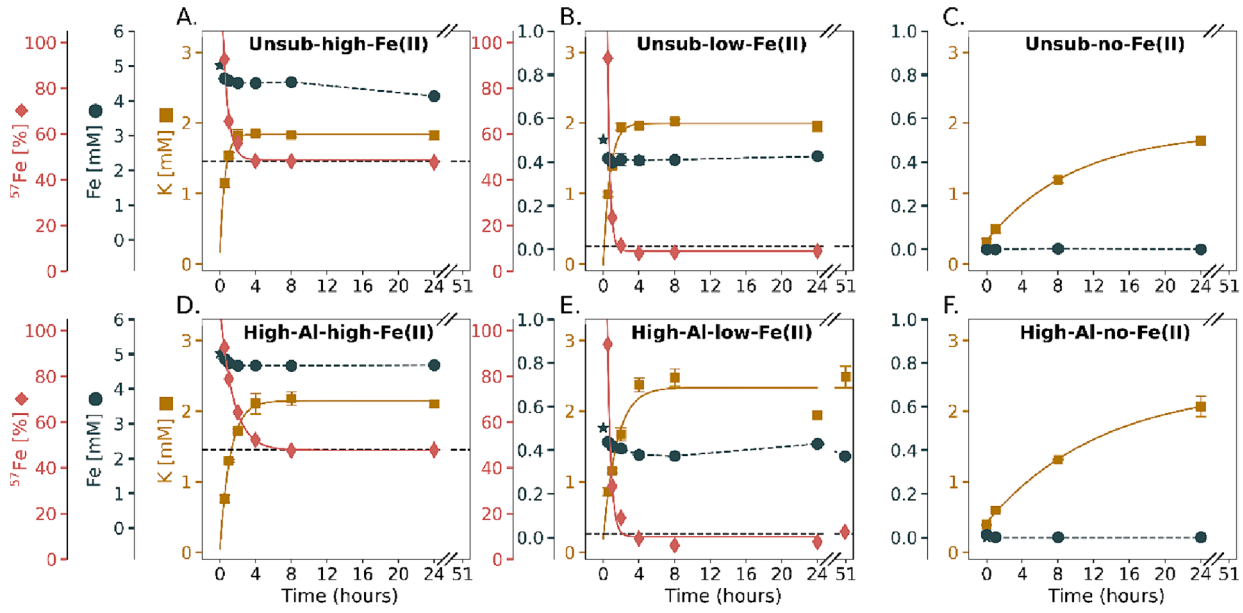

Fig. 2. Concentration of Fe, concentration of K and ^{57}Fe composition of the dissolved Fe pool throughout the transformation experiment in the unsubstituted and high-Al jarosite samples. The plotted curve for K concentration and Fe isotopic composition is a logarithmic function fit to the data points between 0.5 and 24 h. The blue star indicates the theoretical Fe concentration at 0 h based on the concentration of the spike, and black dashed horizontal line indicates the theoretical isotopic ratio of the solution when the system is fully mixed. Error bars are the standard deviation of measurements from three replicate reactors. Data for low-Al and natural jarosite are presented in the Figs. S3, S4 and S5. Note: a discontinuous axis is used to display the sample in the high-Al high-Fe(II) reactor, which was collected at 51 h (the high-Al high-Fe(II) 24-hour datapoint was collected in an independent experiment).

Table 1
Rates of jarosite reaction in XRD Rietveld fitting, K concentration increase in solution and Fe isotope exchange in solution. All rates are calculated assuming pseudo-first-order kinetics and are derived from logarithmic fits of data points (proportion of XRD patterns fitted as jarosite, K concentration in solution and ^{57}Fe/^{tot}Fe in solution, respectively), measured in units of h^{-1} (Section S2.1, S2.2 and S4).

	High Fe(II) spike			Low Fe(II) spike			No Fe(II) spike		
	Jrs reaction [#]	K release	Fe isotope exchange	Jrs reaction [#]	K release	Fe isotope exchange	Jrs reaction	K release	Fe isotope exchange
Unsub	2.4	1.8	1.8	1.7	1.3	3.5	–[†]	0.1	–[*]
Low Al	2.6	1.1	1.8	1.0	0.9	2.9	–[†]	0.1	–[*]
High Al	0.9	0.9	0.9	0.6	0.7	2.5	–[†]	0.1	–[*]
Natural	0.2	0.1	0.2	0.1	0.1	0.5	–[†]	–†	–[*]

[#] The jarosite (Jrs) fit is plotted in Fig. S6 and is not derived from the same procedure as the fitting in Fig. 3.
[*] Not measured in the control experiments because the system was not spiked with ^{57}Fe.
[†] Trend not reliably fit with logarithmic function.

0.01 mM in reactors containing high-Al jarosite (Fig. S4). In the following 24 h, the K concentration in the no-Fe(II) treatments continued to increase with pseudo-first-order rate coefficients of 0.1 h^{-1} for reactors containing unsubstituted, low-Al and high-Al jarosite (Table 1). The release of K before time = 0 indicated that jarosite dissolution began immediately upon suspension in the MOPS solution. However, K dissolution may occur more quickly than jarosite transformation due to incongruous dissolution (Smith et al., 2006; Welch et al., 2007), and therefore the K dissolution rate was not used to calculate jarosite transformation. Results of K release into solution are presented in Section S2.1.

3.2. Rates and products of mineral transformation

Rietveld fitting of XRD patterns (all fitting results in Fig. S6 and selected data in Fig. 3) revealed that lower Al-for-Fe substitution in jarosite and higher Fe(II) concentration were associated with faster jarosite transformation. Changes in the jarosite abundance in XRD patterns were quantified (Table 1) using a pseudo-first-order rate model described in Section S4. The maximum rate of jarosite reaction was 2.4 h^{-1} for the unsubstituted high-Fe(II) treatment. In contrast, the rate of jarosite reaction fell to 1.7 h^{-1} when the Fe(II):Fe(III) ratio was lowered from 1:1 to 1:10, or to 0.9 h^{-1} with an increase in the Al-for-Fe substitution of jarosite up to 7 %. The amount of jarosite remaining one hour after Fe(II) addition provides a useful point of comparison: Jarosite comprised 6 %, 14 %, 35 % and 43 % in the unsubstituted high-Fe(II), unsubstituted low-Fe(II), high-Al high-Fe(II) and high-Al high-Fe(II) reactors, respectively (Fig. S6).

Natural jarosite transformed more slowly than synthetic jarosite, with pseudo-first-order rate coefficients of 0.2 h^{-1} and 0.1 h^{-1} for high and low Fe(II), respectively. Whereas synthetic jarosite was no longer detected by XRD after 2 h in unsubstituted high-Fe(II) reactors and 8 h in high-Al high-Fe(II) reactors, 28 % and 35 % of the initial natural jarosite remained after 24 h in the high-Fe(II) and low-Fe(II) reactors, respectively (Fig. S6). After seven days in the high-Fe(II) treatment, natural jarosite was detectable as a minor phase (approx. 1 %) of the sample mineral composition (data not shown).

Natural and synthetic jarosite also transformed in no-Fe(II) reactors, but the rate was slower than in the reactors containing Fe(II) (Fig. S6). Without Fe(II), 11–15 % of the synthetic jarosite, and 5 % of the natural jarosite, transformed within 1 h. Therefore, between 85 % and 95 % of the initial jarosite was remaining in the reactors after the pre-equilibration period. By t = 24 h, 42–55 % of the synthetic jarosite had transformed, with high-Al jarosite transforming slowest. Further

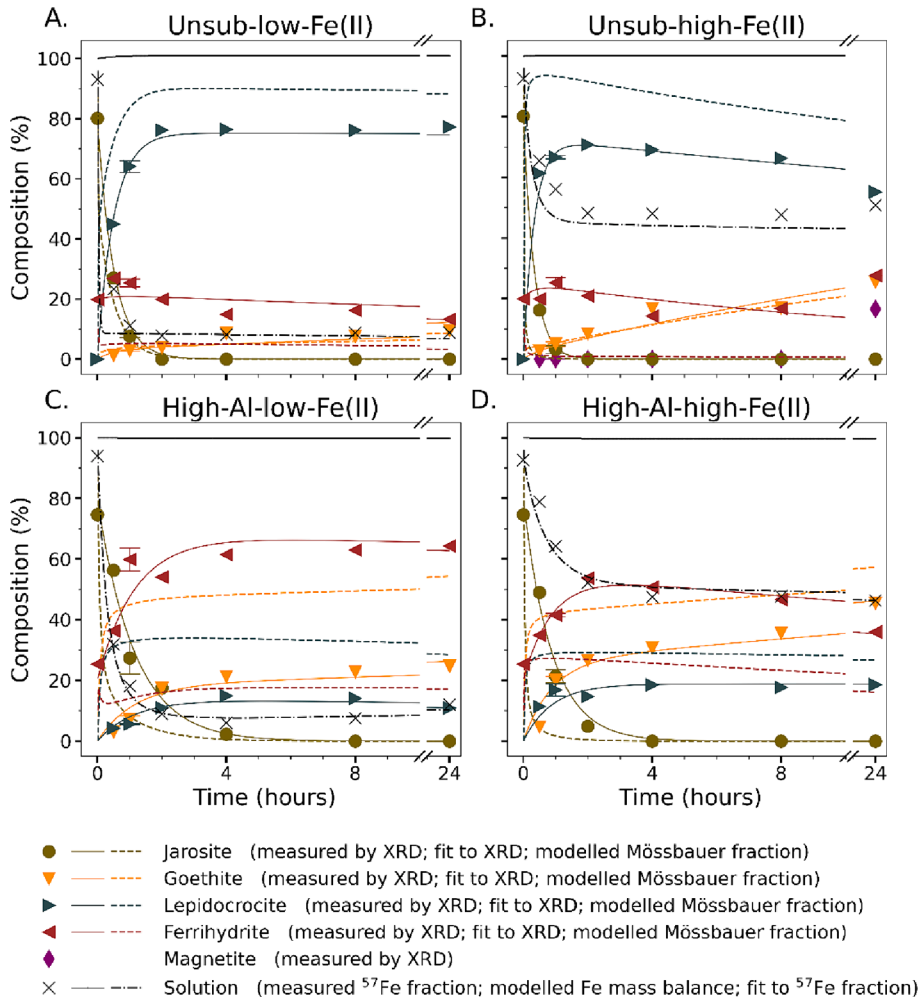

Fig. 3. Composition of the reaction vessels as measured by XRD and calculated by the atom-flow model. The plotted points indicate the fraction of Fe that was bound in each mineral phase, calculated by Rietveld fitting of XRD patterns and adjusted to Fe fraction according to the theoretical Fe molar ratio in each mineral phase (see Section S7.2). The results of Rietveld fitting for all reactors are plotted in Fig. S6. Samples from triplicates reactors were combined before analysis at all timepoints, except after 1 h, where three replicates were measured individually, and the mean and standard deviation (1SD) are plotted. Lepidocrocite detected in one replicate of unsubstituted-no-Fe(II) reactor at 1 h has been omitted from the plot. Solid lines represent the best fit of the XRD measurements within the bounds of the atom-flow model. The dashed lines represent the fraction of ^{57}Fe in each mineral phase as calculated by the atom-flow model.

transformation of natural jarosite was not detectable between t = 0 and t = 24 in no-Fe(II) reactors.

The products of jarosite transformation were ferrihydrite, lepidocrocite and goethite, with <20 % magnetite formed between the 8- and 24-hour timepoints in unsubstituted high-Fe(II) and low-Al high-Fe (II) reactors (Fig. S6). A higher proportion of ferrihydrite in the products was associated with greater Al substitution in jarosite and lower Fe(II) concentrations. Indeed, ferrihydrite was the major product in no-Fe(II) reactors (with some goethite <5 %) and comprised as much as 64 % of the total mineral composition in the high-Al high-Fe(II) reactors. Goethite was observed in all reactors with Fe(II) and reached as much as 46 % after 24 h in the high-Al high-Fe(II) reactors. Lepidocrocite was the predominant transformation product of low-Al jarosite, which formed up to 77 % of the total mineral after 24 h in unsubstituted low-Fe(II) reactors (Fig. S6). Natural jarosite transformed into roughly similar proportions of ferrihydrite, lepidocrocite and goethite.

3.3. Mineral properties during transformation

The shape, size and relative arrangement of synthetic jarosite and its transformation products were investigated in partially transformed jarosite samples, by analysing secondary electron (SE) images of mineral samples from unsubstituted high-Fe(II) (Fig. 4A-D) and high-Al high-Fe (II) (Fig. 4E-F) reactors at t = 1 h. The primary particles largely corresponded to the size (2–4 μm diameter) and spherical form of the initial jarosite minerals (c.f. Fig. S17 and Fig. 4A & E). However, the primary particles were covered in new crystal phases, some resembling the 'frost-like' or 'hedgehog-like' coatings (e.g. Fig. 4A and 4E) and lepidocrocite lathes (e.g. Fig. 4B) observed in previous studies (Johnston et al., 2012; Smith et al., 2006; ThomasArrigo et al., 2019). Further examples of lepidocrocite lathes were observed in Fig. 4C and S20. Ferrihydrite, which usually takes the form of aggregations of smaller particles, approx. 5 nm in diameter (Grigg et al., 2022; ThomasArrigo et al., 2019), could explain some of the small particles in SE images (e.g Fig. 4D), consistent with its detection by XRD among the transformation products of jarosite. In reactors containing unsubstituted jarosite, the larger crystals growing on the surface of the primary particles had platey form (Fig. 4A & 4B), and the smaller crystals (approx. 50 nm length; Fig. 4A & 4B) had needle form, which may correspond to previously-identified crystal forms of lepidocrocite and goethite, respectively (Grigg et al., 2022).

Natural jarosite occurred in smaller particles than synthetic jarosite, approximately 1 μm in diameter (Fig. S17). Furthermore, the SE images (Fig. 4G & 4H and Fig. S22) and elemental distribution maps (Fig. S23)

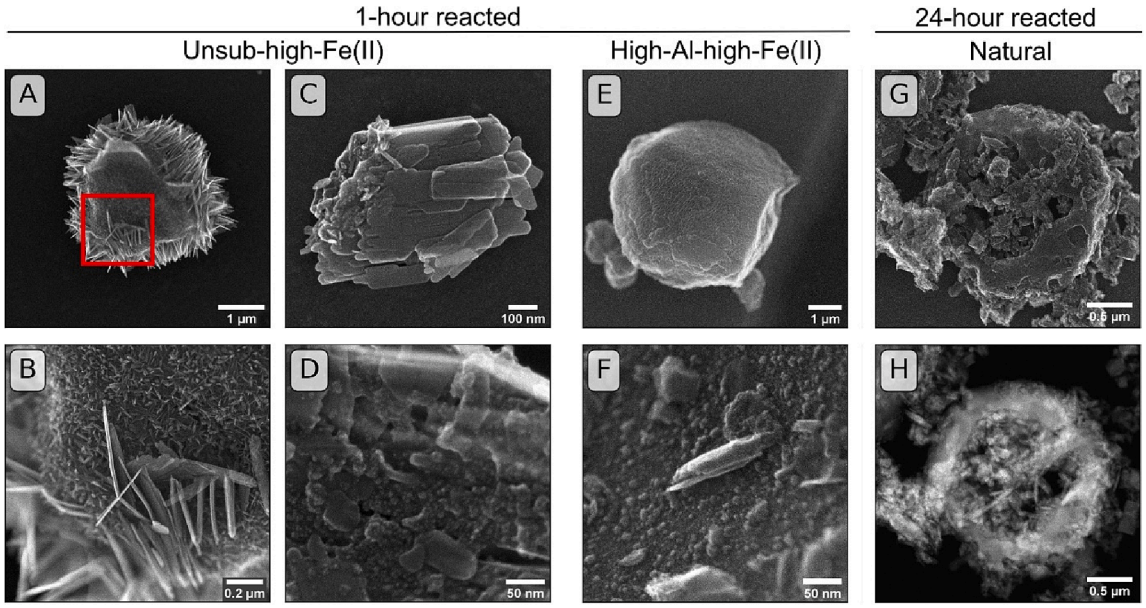

Fig. 4. Electron microscope images of reacted minerals. Panels A, B, C & D: Secondary electron (SE) images of unsubstituted jarosite, reacted with high Fe(II) treatment for one hour. Panel B is taken from the region marked with a red box in panel A. Panel C is reproduced as Fig. S20 with selected angles measured. Panels E and F: SE images of minerals sampled from a high-Al high-Fe(II) reactor at the one-hour timepoint. Panel G: An SE image of natural jarosite after 24 h of reaction with high Fe(II). Panel H: High-angle annular dark field image (HAADF) of the same particle shown in panel G. Additional SE/HAADF image pairs of reacted natural jarosite samples are presented in Fig. S22. SE images of unreacted minerals are presented in Fig. S17.

collected on 24-hour reacted samples of natural jarosite revealed complex mineral aggregates. A particle structure that was commonly observed comprised K-, S- and Fe-rich spherical shells, which were consistent with jarosite, and Fe-rich and K- and S- deficient interiors, which were consistent with Fe oxyhydroxides. The aggregates were further permeated by small Al- and Si- rich phases, consistent with clay or secondary Al mineral phases.

Rietveld fitting of the XRD patterns showed that the unit cell size of

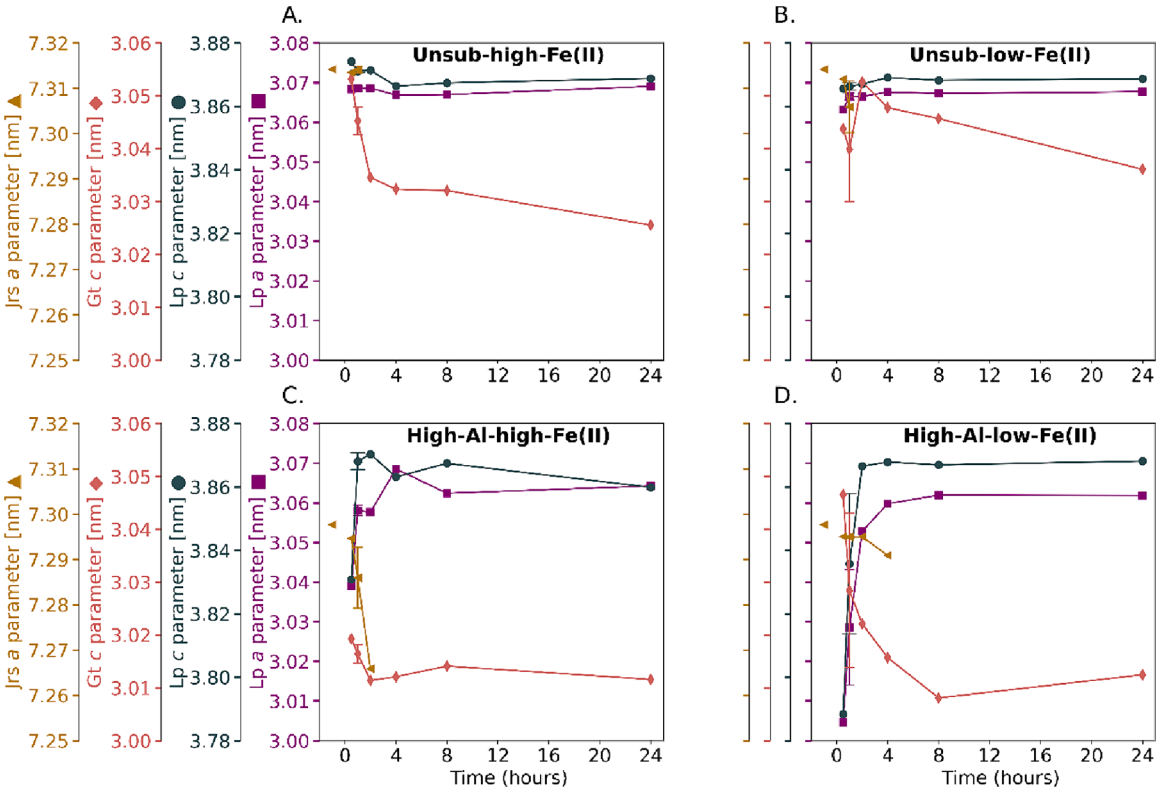

Fig. 5. Selected unit cell sizes for jarosite and products during the transformation reaction. Samples from replicate reactors were combined before analysis at all time points, except for the 1-hour timepoint, when individual replicates were measured, and the mean and standard deviation (1SD) plotted as error bars. Full data sets including measurements from all reactors and all unit cell dimensions are plotted in Figs. S7–S13.

jarosite, lepidocrocite and goethite varied over the course of the experiment (Fig. 5). The average size of the *a* dimension of the jarosite unit cell, which is strongly affected by substitution at the B site (Grigg et al., 2024), was initially smaller in Al-jarosite than unsubstituted jarosite. As Al-jarosite transformed, the *a* unit cell dimension of the remaining Al-jarosite also decreased, particularly in the high-Al high-Fe (II) treatment (from 7.2977 Å in the initial mineral sample to 7.2658 Å at 2 h; Fig. 5). By contrast, the unit cell was unchanged in unsubstituted jarosite. The average lepidocrocite unit cell dimensions were constant in reactors without Al (Fig. 5). The lepidocrocite that formed in high-Al reactors initially had smaller *a* and *c* dimensions than lepidocrocite that formed in reactors containing low-Al or unsubstituted jarosite, but within 2–4 h the unit cell of high-Al jarosite grew to resemble the unit cell size of lepidocrocite formed in reactors containing low-Al or unsubstituted jarosite (Fig. 5). The *b* dimension was not related to Al content of the lepidocrocite. In goethite, the *a*, *b* and *c* dimensions changed over time after goethite formation (*c* dimension in Fig. 5 and all dimensions in Figs. S11–S13). The effect is illustrated by the *c* dimension, which decreased over time in all treatments, but was smallest after 24 h in high-Al reactors (from 3.0193 Å after 0.5h to 3.0116 Å at 24 h).

Although the crystallite sizes also differed according to the amount of Al in the system, the temporal patterns were not associated with the Al content. The largest differences were observed in lepidocrocite, which showed prominent crystal growth in the [1 1 1] direction in reactors containing unsubstituted and low-Al jarosite but did not preferentially grow on any measured crystal plane in high-Al reactors. Details about the mineral crystallite sizes are available in Section S3.3.

Some trends in mineral structure and substitution could be ascertained by analysis of the location of Raman spectral peaks. Aluminium-for-Fe substitution of jarosite is linked to the position of the Raman spectral peak near 301 cm^{-1} (O-Fe) and near 625 cm^{-1} ($\nu_4(SO_4)$) (Grigg et al., 2024). The position of the jarosite O-Fe peak (Fig. S24) was not interpreted due to interference from the spectrum of goethite (Grigg et al., 2024). Changes of the $\nu_4(SO_4)$ position in low-Al high-Fe(II) and high-Al high-Fe(II) reactors are consistent with increasing Al content over time (Fig. S25). A strong trend was also observed in the location of the peak near 530 cm^{-1} (Fig. S26), which corresponds to the Raman spectrum of lepidocrocite. The peak position was consistent over time in unsubstituted jarosite samples and decreased over time in low-Al jarosite samples.

3.4. Mineral transformation processes

The distribution of ^{57}Fe was used to trace which processes had led to the observed mineral composition in the reactors. In a first analysis step, the Mössbauer spectra collected at 4.2 K were fit with four phases (Fig. S28 and Table S2), each with locked model parameters representing jarosite (Grigg et al., 2024), ferrihydrite (ThomasArrigo et al., 2018), goethite (Notini et al., 2022) and lepidocrocite (Schulz et al., 2023). The fits of spectra from reactors containing unsubstituted jarosite were dominated by lepidocrocite (58 % and 61 % in low- and high-Fe(II) reactors, respectively), with smaller areas attributable to ferrihydrite, goethite and jarosite (Table S3). In the high-Al spectra, lepidocrocite was less abundant (19 % and 25 % in low- and high-Fe(II) reactors, respectively) whereas ferrihydrite and goethite were most abundant (up to 43 % ferrihydrite in the high-Al high-Fe(II) reactor; Table S3). The variability of the hyperfine characteristics of the minerals (see Table S5 for summary of variability reported in the literature) may have contributed to a small misfit in Fig. S28 and affected the fitted areas of each phase. Both spectra collected at 4.2 K and 77 K were also fitted with floating parameters (Table S4). This approach provided the most effective analysis of spectra collected at 77 K. However, due to overlap of the mineral phases in 4.2 K spectra and poor magnetic ordering of some phases at 77 K, the identity of each fitted curve was difficult to interpret, and each phase likely included parts of multiple minerals. The results of the Mössbauer spectral fitting using floating parameters are described in Section S6.3.

To interpret which processes caused the observed differences between the ^{57}Fe distribution in the Mössbauer spectra and mineral distribution in XRD measurements, the measurements were analysed with reference to a model of atom flow through a conceptual reaction space. In high-Al reactors, the atom-flow model suggested that ^{57}Fe was enriched in goethite and lepidocrocite but depleted in ferrihydrite. The atom-flow model produced reasonable agreement with the mineral composition measured by XRD (Fig. 3) and the reconstructed Mössbauer spectra generally agreed with the measured spectra (Fig. 6). The largest difference was that calculated ^{57}Fe content of the ferrihydrite was lower than measured in the Mössbauer spectrum, coupled with a higher estimation of the ^{57}Fe in goethite and lepidocrocite. Ferrihydrite comprised 14 % and 27 % of the ^{57}Fe in the reconstructed spectra of low-Fe(II) and high-Fe(II) reactors, respectively, but 43 % and 34 % in the fitted spectra, respectively (Table S3, Table S7 and Fig. S29). In reactors containing unsubstituted jarosite, the fits of XRD measurements were associated with higher residual error than fits from high-Al reactors (Table S6). Notwithstanding the uncertainties inherent in fitting ferrihydrite in XRD patterns using the PONKCS method (see details in Section S3.1; Aeppli et al., 2019; Schulz et al., 2022; ThomasArrigo et al., 2018), the misfit between the measured and modelled total Fe distribution occurred because there was rapid transformation of ferrihydrite between 1 and 4 h after the addition of Fe(II) to reactors containing unsubstituted jarosite, which could not be captured by the processes defined in the conceptual model (Fig. 1). In addition, the reconstructed Mössbauer spectra from reactors containing unsubstituted jarosite did not effectively reproduce prominent features of the measured 4.2 K Mössbauer spectra (Fig. 6). The difference between the reconstructed and measured spectra were caused by the large proportion of ^{57}Fe in lepidocrocite calculated by the atom-flow model (84 % and 93 % of all ^{57}Fe in low-Fe(II) and high-Fe(II) rectors, respectively; Table S7), and consequently small fractions of minerals with large hyperfine field (H), particularly goethite (Table S2).

The differences between the reconstructed and measured Mössbauer spectra indicated that some processes occurred in the reactors which were not captured by the conceptual model. Some processes that were excluded from the model, including formation of magnetite, Fe(II)-catalysed recrystallisation of goethite (Joshi et al., 2022; Pedersen et al., 2005; Williams and Scherer, 2004), Fe(II)-catalysed recrystallisation of ferrihydrite to lepidocrocite (Hansel et al., 2011), and formation of inhomogeneous mineral pools (Joshi et al., 2022); were considered not to be the most likely causes of the misfits. The details of these model design choices are discussed in Section S7.2. A summary of the comparison between XRD-based measurement of Fe distribution, fitting of Mössbauer spectra and ^{57}Fe distribution calculated by the atom-flow model are summarised in Fig. S29.

The ^{57}Fe enrichment in each reactor gradually approached a steady value as the Fe in solid and solution mixed throughout the course of the experiment. After one hour, the ^{57}Fe composition of the solution was furthest from its steady value in high-Al high-Fe(II) reactors where the isotopic ratio at 1 h, $\frac{[^{57}Fe]_1}{[Fe]_1}$, was 0.64, whereas the ratio after 24 h, $\frac{[^{57}Fe]_{24}}{[Fe]_{24}}$, was 0.46, and theoretically, the ratio in the total system, $\lim_{t\to\infty}\frac{[^{57}Fe]}{[Fe]}$, was 0.48 (Fig. 2; calculations Section S2.2). The solution in the unsubstituted high-Fe(II) reactors approached a steady value at double the rate of the high-Al reactor due to faster jarosite transformation, with $\frac{[^{57}Fe]_1}{[Fe]_1} = 0.56$. Isotopic ratios initially approached their steady value fastest in low-Fe (II) reactors, as the aqueous Fe(II) is a relatively small pool of Fe(II) in low-Fe(II) systems that turns over more quickly. Note, the steady value may not be the same as the system equilibrium when recalcitrant solid phases are enriched or depleted in ^{57}Fe. Indeed, the aqueous-phase isotopic ratio briefly fell below the equilibrium at the 2-, 4- and 8-hour timepoints, indicating that isotopic imbalances existed in low-Al systems until at least 8 h. Overall, the isotope balance at the one-hour

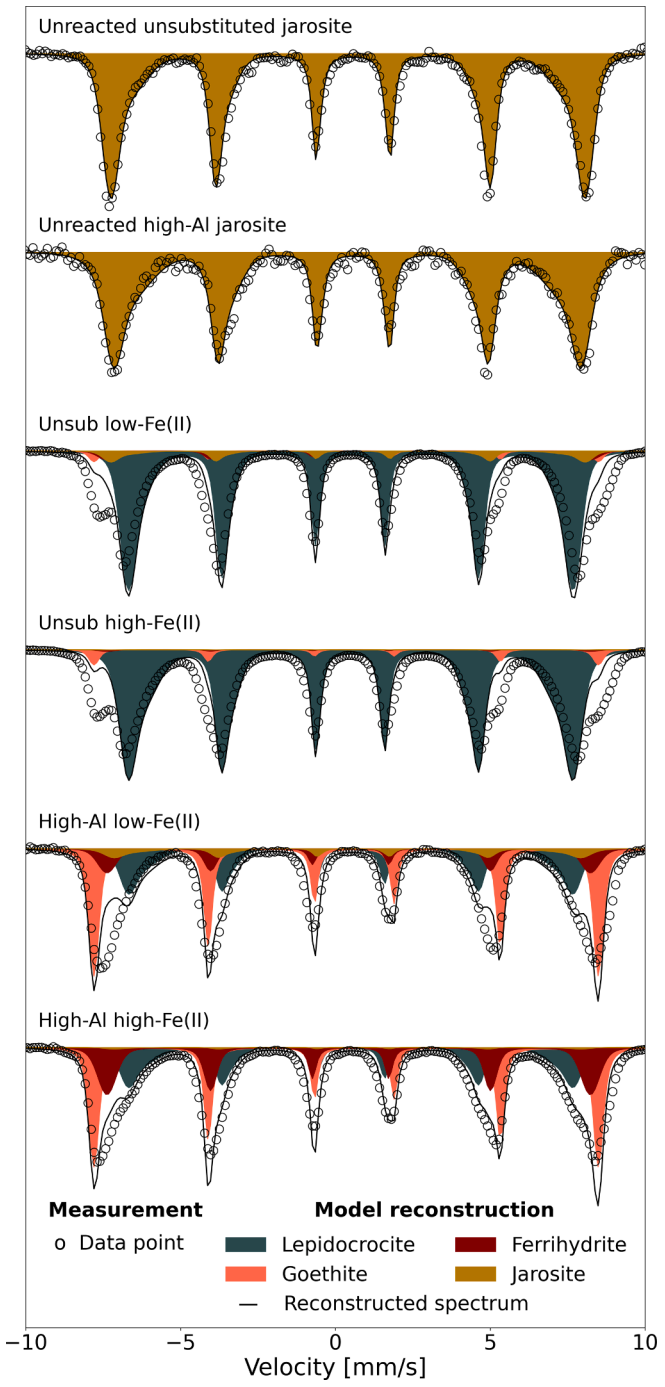

Fig. 6. Comparison of Mössbauer spectra, collected at 4.2 K, of unsubstituted and high-Al synthetic jarosite before the transformation and mineral samples following one hour of reaction in low-Fe(II) or high-Fe(II) conditions. All plotted data are normalised by the total fitted area. The solid black line is the sum of the coloured regions, which represent a reconstruction of the spectrum based on the relative area of each phase as calculated by the atom-flow model (Fig. 3 and Table S7), and model spectral parameters for jarosite (Grigg et al., 2024), ferrihydrite (ThomasArrigo et al., 2018), goethite (Notini et al., 2022), and lepidocrocite (Schulz et al., 2023) (Table S2).

timepoint was most suitable for assessing the reaction pathways in high-Al reactors, due to the lower rate of isotope exchange.

4. Discussion

4.1. Effects of Al substitution on jarosite transformation rate and products

4.1.1. Effects on jarosite

The rate of jarosite transformation in the presence of Fe(II) was strongly related to the initial mineral composition, whereby Al-for-Fe substitution stabilised jarosite against transformation. Aluminium slowed the transformation by almost a factor of three despite the marginally lower crystallinity of the Al-substituted jarosite (crystallite sizes of unsubstituted and high-Al jarosite were 95 nm and 88 nm, respectively, Grigg et al., 2024). The result was consistent with previous studies of Fe oxyhydroxides, which have shown that Al-for-Fe substitution slows the Fe(II)-catalysed transformation of ferrihydrite to goethite, lepidocrocite and magnetite (Masue-Slowey et al., 2011), and that Al-for-Fe substitution of goethite results in slower atom exchange with aqueous Fe(II), Fe(II)-catalysed transformation and release of incorporated trace elements (Frierdich et al., 2012; Latta et al., 2012). Further, the effect of Al-for-Fe substitution on the rate of transformation in the presence of Fe(II) was strong in comparison to changes in the Fe (II) concentration in the system. An order-of-magnitude increase in the Fe(II) concentration was associated with approximately a 50 % increase in the rate of jarosite reaction in reactors containing unsubstituted and high-Al jarosite, consistent with the previously reported 100 % increase in jarosite reaction rate caused by a 20-times increase in Fe(II) concentration (Karimian et al., 2017), which mirror the effect of Fe(II) on other Fe mineral phases (Grigg et al., 2022; Hansel et al., 2005).

In contrast to the transformation of jarosite in the presence of Fe(II), the rate of decomposition by hydrolysis (in reactors without an Fe(II) spike) was similar in unsubstituted and high-Al treatments. Whereas 42 % of the high-Al jarosite transformed within 24 h, 55 % of the unsubstituted jarosite transformed within the same period. The reaction in the presence of Fe(II) may be dominated by Fe(II)-catalysed transformation, likely involving the conduction of electrons through the crystal structure as observed for Fe oxyhydroxides such as ferrihydrite or goethite (Gorski and Scherer, 2011), whereas hydrolysis is a surface reaction that may be less influenced by the presence of Al in the mineral structure. End-member alunite is known to dissolve at least two orders of magnitude more slowly than jarosite, possibly due to the rate of exchange of water with Fe or Al cations at the mineral surface (Miller et al., 2016), but the magnitude of the effect in mineral containing both Fe and Al may be much smaller.

As Al was not detected in solution, the fate of Al during the transformation of Al-substituted jarosite depended on the solid phases. The fate of Al could be followed by observing changes in the structural characteristics of minerals over the course of the experiments. In high-Al low-Fe(II) and high-Al high-Fe(II) reactors, the decreasing size of the a dimension of the jarosite unit cell (Fig. 5), and the shift of the jarosite $\nu_4(SO_4)$ Raman peak (Fig. S25) to lower wavenumbers, are both consistent with progressively higher Al content in jarosite (Grigg et al., 2024). By contrast, in reactors containing unsubstituted jarosite and high-Al no-Fe(II) conditions, variation in jarosite unit cell dimensions and $\nu_4(SO_4)$ Raman peak position were not observed, indicating that the average Al content of jarosite does not change during hydrolysis. Aluminium may have been enriched in jarosite by an incongruous dissolution mechanism, which has been observed for other metals substituted in jarosite (Chen et al., 2021), and would be consistent with the low solubility of Al(III) at circumneutral pH. It is possible that the Al enrichment of the jarosite phase contributed to the slower rate of Al-jarosite transformation compared with unsubstituted jarosite transformation.

4.1.2. Effects on the products of transformation

In reactors containing Al, lepidocrocite formation was hindered in favour of goethite. A similar effect of Al on lepidocrocite formation was previously observed during the aeration of solutions containing Fe(II) and Al (Taylor and Schwertmann, 1978), and during transformation of Al-substituted ferrihydrite (Hansel et al., 2011). As well as altering the product composition, there is strong evidence that Al-for-Fe substitution in lepidocrocite altered the structure and morphology of the lepidocrocite formed during Al-substituted jarosite transformation. At least 18.5 % Al-for-Fe substitution of lepidocrocite is possible (Liao et al., 2020) and Al-substituted lepidocrocite has smaller crystallites (Poulton et al., 2004), has a smaller unit cell in all three dimensions (Liao et al., 2020; Schwertmann and Wolska, 1990) with the largest and most consistent difference in *a* and *c* dimensions (Liao et al., 2020). In our high-Al reactors, lepidocrocite had a smaller crystallite size and unit cell size in the *a* and *c* dimensions than lepidocrocite that formed in reactors containing unsubstituted jarosite throughout the experiment (Figs. 5 and S22). By applying the relationship between *a* and *c* parameters and Al substitution derived by Liao et al. (2020), samples of lepidocrocite taken at 30 min may have contained 9.1 % or 9.5 % (based on *a* and *c* parameter, respectively) Al-for-Fe substitution in the low-Fe(II) high-Al reactors and 19.2 % or 17.6 % (based on *a* and *c* parameter, respectively) Al-for-Fe substitution in the high-Al high-Fe(II) reactors. Applying the same calculation to reactors containing unsubstituted jarosite predicts Al-for-Fe substitution between 0.5 % and 2.7 %, indicating a small systemic difference between the measurements in this study and Liao et al. (2020). Additional evidence of Al-for-Fe substitution in lepidocrocite is provided by measurements of crystal morphology and crystallite size. Aluminium substitution of lepidocrocite is associated with thinner, shorter and wider lath structures (Hansel et al., 2011; Liao et al., 2020). In SE images of 1-hour reacted samples, platey minerals that were attributable to lepidocrocite appeared to be smallest in high-Al reactors (c.f. Fig. 4A and 4E). Furthermore, XRD analysis showed that crystal growth was restricted in the [1 1 1] direction in high-Al reactors, compared to the elongated crystals in the [1 1 1] direction that were able to grow in reactors containing unsubstituted and low-Al jarosite. Although the effect of Al on the Raman spectra of lepidocrocite is not documented, larger wavenumbers generally correspond to higher Al substitution in Fe minerals such as jarosite (Grigg et al., 2024) and goethite (Liu et al., 2013) and therefore the trends observed in Raman spectral peaks support the interpretation that lepidocrocite in high-Al reactors was initially enriched in Al. The XRD- and Raman-based indicators of Al substitution in lepidocrocite changed during the first 2–4 h of reaction, which demonstrate temporal shifts in the average Al content of lepidocrocite. The evolution could indicate that lepidocrocite continued to react and release Al after its initial formation, or that the Al incorporation into lepidocrocite reduced over time.

The unit cell parameters of goethite also provide evidence for Al substitution. The *b* and *c* dimensions of the goethite unit cell are linearly correlated to Al-for-Fe substitution (Schulze, 1984). Therefore, the smaller size of the *b* and *c* dimensions of the goethite unit cell in our high-Al systems (Figs. 5 and S12) may indicate that Al was incorporated into goethite. By applying a previously derived correlation between the *c* parameter and Al-for-Fe substitution (Schulze, 1984), the Al-for-Fe substitution of goethite at the 24-hour timepoint could be estimated at 7.4 % in the high-Al high-Fe(II) reactors and 6.8 % in the high-Al low-Fe (II) reactors. However, the predicted Al content of −6.6 % and −0.6 % in unsubstituted-jarosite reactors indicate that the measured *c* lengths of the product goethite was larger than that of the former synthetic goethite, and may not be directly applicable here (Schulze, 1984). Although Raman spectral peak positions may also depend on Al substitution in goethite (Liu et al., 2013), spectral peaks associated with goethite were either not strong enough to reliably fit in the mixed reacted mineral spectra or were not easily distinguishable from the peaks of other mineral phases (the peak near 242 cm^{-1} is near a lepidocrocite peak, and the peak near 299 cm^{-1} is near a jarosite peak). Temporal trends of goethite unit cell size and crystallite size from XRD Rietveld analysis are similar in all reactors (Figs. S11–13 and S16) and do not depend on the Al content of the reactors.

There was no direct evidence that Al substitution of ferrihydrite occurred following transformation of Al-substituted jarosite. However, ferrihydrite was a more abundant product of the transformation processes in high-Al rectors. This may indicate that Al promoted the formation of poorly crystalline products such as ferrihydrite, as suggested by the higher k_1 and k_3 in the isotope model (Table S6), or that Al stabilised the ferrihydrite against transformation (Taylor and Schwertmann, 1978).

4.2. Differences between synthetic and natural jarosite transformation

The transformation of natural jarosite proceeded more slowly than the transformation of synthetic jarosite in reactors with comparable solution composition. The Al-for-Fe substitution of the natural jarosite was approximately 5 % (Grigg et al., 2024), which was most similar to the Al content of the high-Al synthetic jarosite. However, other differences in the natural and synthetic jarosite crystal structures may explain the difference. Natural jarosite had higher total B-site occupancy than the synthetic jarosite, as evidenced by the higher blocking temperature and larger quadrupole shift (ε) in Mössbauer spectra (Grigg et al., 2024), which could have contributed to its stability. Furthermore, the synthetic jarosite contained more A-site deficiencies that were likely filled by hydronium (Grigg et al., 2024). Hydronium-jarosite dissolves faster than K-jarosite (Gasharova et al., 2005), and may also be more reactive in our experimental systems.

In additional to crystal composition, some difference between the natural and synthetic jarosite reactivity may be explained by particle morphology (Gasharova et al., 2005). The synthetic jarosite occurred as spheres (Grigg et al., 2024). In contrast, the natural jarosite in this experiment displayed octahedral and tabular form (Fig. S17; Grigg et al., 2024), consistent with previously recorded natural jarosite (Mees and Stoops, 2018). The morphology of natural jarosite could represent more mature crystal forms that are resistant to transformation, or could indicate that the jarosite formed as a pseudomorph of pyrite (Carson et al., 1982). The 24-hour reacted natural jarosite retained a hexagonal shape, but mineral products of the natural jarosite transformation were observed inside the jarosite particles (Figs. 4G, 4H, S22 and S23). Recrystallisation of the interior of natural jarosite particles stood in direct contrast to the formation of secondary products on the exterior of synthetic jarosite particles. The apparent growth of products in the interior may be explained by jarosite transformation occurring on crystal faces that preferentially lay perpendicular to the electron beam. Analysis of elemental distribution by EDX did not indicate a surface enrichment of compounds that could passivate the faces, such as Al, Si or C compounds (Fig. S23). The stability of the crystal faces that remained untransformed could account for the overall slower rate of natural jarosite transformation.

4.3. Pathways of mineral transformation

4.3.1. Sources of jarosite

Jarosite was initially composed of ^{NA}Fe, but recrystallisation of jarosite by atom exchange with aqueous ^{57}Fe would have caused an increase in the ^{57}Fe content of jarosite. Indeed, there is some evidence that ^{57}Fe-enriched jarosite formed in low-Fe(II) reactors. The initial fraction of the total ^{57}Fe contained in jarosite in low-Fe(II) reactors was 18 %, while only 14 % and 43 % of the initial jarosite remained after one hour in unsubstituted low-Fe(II) and high-Al high-Fe(II) reactors, respectively. Therefore, the theoretical proportion of ^{57}Fe contained in the remainder of the initial ^{NA}Fe-jarosite was 3 % and 8 % in reactors containing unsubstituted and high-Al jarosite, respectively. By comparison jarosite explained 11 % and 15 % of the 4.2 K Mössbauer spectra from unsubstituted low-Fe(II) and high-Al high-Fe(II) reactors, respectively

(Table S3), and similar amounts in the fits of 77 K spectra (Table S4). Correspondingly, a non-zero rate of ^{57}Fe-jarosite formation was calculated in the atom-flow model (rate coefficient k_9 in Table S6), showing that jarosite recrystallisation was a slow process in comparison to the dissolution or Fe(II)-catalysed transformation of jarosite in the high-Al reactors, but faster than hydrolysis in the unsubstituted low-Fe(II) reactors (c.f. coefficients k_9, k_1 and k_2 in Table S6). In the high-Fe(II) reactors, the evidence for jarosite recrystallisation was less clear, possibly due to the higher rate of jarosite transformation to other minerals. In unsubstituted high-Fe(II) reactors, jarosite was absent from the Mössbauer fits, and therefore the isotope composition of the jarosite could not be analysed (Tables S3 and S4). In high-Al high-Fe(II) reactors, process k_9 was fit as zero, indicating no formation of ^{57}Fe-jarosite, and less than 2 % of the spectrum was fit as jarosite, consistent with the theoretical ^{57}Fe content of the remaining initial ^{NA}Fe-jarosite.

4.3.2. Sources of ferrihydrite

Ferrihydrite is a poorly crystalline product of both the hydrolysis reaction and Fe(II)-catalysed transformation of jarosite. In no-Fe(II) reactors, synthetic jarosite was converted to 43–58 % ferrihydrite by the end of the experiment (t = 24 h), but faster ferrihydrite formation was observed in the presence of Fe(II). Although the effect of hydrolysis was masked by Fe(II)-catalysed transformations in reactors containing Fe(II), the atom-flow model was designed to deconvolute the processes (rate coefficients k_1 and k_3). The atom-flow model indicated that Fe(II)-catalysed transformation was the only meaningful formation pathway of ferrihydrite in the reactors containing unsubstituted jarosite and high Fe(II), leading to a relative depletion of ^{57}Fe. In high-Al low-Fe(II) reactors, the rate of hydrolysis was greater than the rate of Fe(II)-catalysed transformation (0.493 and 0.017 h^{-1}, respectively; Table S6), which also led to a relative depletion of ^{57}Fe (14 % of ^{57}Fe in solid phases at one hour; Table S7). By contrast, the two transformation processes had similar rates in the high-Al high-Fe(II) system (0.259 and 0.231 h^{-1}, respectively; Table S6), leading to a smaller relative depletion of ^{57}Fe (27 % of ^{57}Fe in solid phases at one hour; Table S7). The amount of ferrihydrite fit in the Mössbauer spectra from high-Al reactors (Table S3 and S4) was higher than that calculated by the atom-flow model, especially in the high-Al high-Fe(II) reactor. This could indicate that not all atom flows were accounted for in the atom-flow model. The possibility of a heterogeneous mixing model to explain the behaviour of ferrihydrite is discussed in Section S7.3.

4.3.3. Sources of goethite

The general form of the Mössbauer spectra from high-Fe(II) and low-Fe(II) reactors were similar to one another, at both collection temperatures and all Al contents (Fig. 6), emphasising the similarity of the jarosite reaction pathways that occurred despite the one-order-of-magnitude difference in the Fe(II) concentration. The most notable difference between the high-Fe(II) and low-Fe(II) Mössbauer spectra is the size of the magnetically ordered (sextet) fraction at 77 K, which was largely consistent with goethite (Larese-Casanova et al., 2010; Wan et al., 2017). This phase comprised 19 % and 29 % of the spectrum in unsubstituted low-Fe(II) and unsubstituted high-Fe(II) reactors, respectively, and 9 % and 21 % of high-Al high-Fe(II) and high-Al high-Fe(II) spectra, respectively (Table S4). These fits were broadly consistent with the amount of goethite fit in the 4.2 K spectra using reference parameters (Table S3). Moreover, the fits of Mössbauer spectra collected at 4.2 K and 77 K contained larger proportions of goethite than was measured by XRD (Fig. S29), suggesting that goethite was enriched in ^{57}Fe due to formation from Fe that was initially in solution.

In the high-Al reactors, the atom-flow model indicated that the Fe(II)-catalysed transformation of jarosite to goethite accounted for most goethite formation, at a rate that increased with greater Fe(II) concentration (coefficient k_4 increased from 0.200 to 0.369 h^{-1}; Table S6). The atom-flow model indicated that Fe(II) also increased ferrihydrite and lepidocrocite formation rates and contributed to their onward transformation to goethite. However, goethite formation from secondary mineral transformation was limited in comparison to the direct Fe(II)-catalysed transformation of jarosite to goethite (Table S6, coefficient k_7, 0.011 – 0.028 h^{-1}). The formation of goethite from jarosite, ferrihydrite and lepidocrocite could have proceeded by a mechanism similar to that previously proposed for the Fe(II)-catalysed transformation of ferrihydrite, whereby reductive dissolution of Fe in the transforming mineral is coupled to the oxidation of Fe(II) in solution to a labile Fe(III) compound that nucleates goethite or lepidocrocite by a process of oxolation or olation (Sheng et al., 2020). Higher Fe(II) concentrations were also associated with an increased fraction of goethite in the products in unsubstituted, low-Al and high-Al systems, consistent with the findings from previous studies of Fe(II)-catalysed jarosite transformation (Karimian et al., 2017), and also promoted transformation of goethite to magnetite in reactors containing low-Al and unsubstituted jarosite. The formation of goethite by the Fe(II)-catalysed process is the major reason for the enrichment of ^{57}Fe in the goethite phase.

4.3.4. Sources of lepidocrocite

Fitting of both the XRD patterns and Mössbauer spectra collected at 4.2 K indicated that lepidocrocite was the major product of unsubstituted or low-Al jarosite transformation. Lepidocrocite may contain ^{57}Fe due to the formation of lepidocrocite from Fe(II) in solution, by Fe(II)-catalysed transformation of existing jarosite or by Fe(II)-catalysed transformation of Fe oxyhydroxides. However, the isotope model predicted an enrichment of ^{57}Fe in the lepidocrocite phase that could not be reconciled with the measured Mössbauer spectra (Fig. 6). Whereas the isotope model predicted a lepidocrocite content of 84 % and 93 % in unsubstituted low-Fe(II) and unsubstituted high-Fe(II) Mössbauer spectra, respectively (Table S7), the fits of Mössbauer spectra collected at 4.2 K fit 58 % and 61 % lepidocrocite, respectively (Table S3). By comparison to the lepidocrocite fit in XRD patterns (60 % and 65 % in unsubstituted low-Fe(II) and unsubstituted high-Fe(II) XRD patterns, respectively), the fraction of lepidocrocite in the Mössbauer spectra represents no more than a modest enrichment of ^{57}Fe. In high-Al reactors, Mössbauer spectra confirmed that lepidocrocite was a less significant product of transformation than in reactors containing unsubstituted jarosite. In these spectra, lepidocrocite was not abundant enough to produce a peak distinct from the other Fe(III) magnetically ordered phases in spectra collected at 4.2 K (Fig. 6). As in the unsubstituted-jarosite reactors, lepidocrocite was predicted by the atom-flow model to have a strong ^{57}Fe enrichment. However, the proportion of the 4.2 K Mössbauer spectrum fit as lepidocrocite was only marginally more than the proportion of lepidocrocite in the XRD Rietveld fits (Fig. S29).

The calculated ^{57}Fe enrichment of lepidocrocite in the atom-flow model is a direct result of its formation exclusively from atoms in the solution. Therefore, lower ^{57}Fe enrichment in lepidocrocite than calculated by the atom-flow model may indicate that some atoms in lepidocrocite did not come from the solution. Lepidocrocite may have formed directly from ^{NA}Fe in jarosite, perhaps during jarosite dissolution, or via rapid transformation of ^{NA}Fe-ferrihydrite by a pathway that did not include Fe exchange with the solution. Direct transformation of jarosite to lepidocrocite without oxidation of $Fe(II)_{aq}$ to form the lepidocrocite has been previously hypothesised in the presence of sulfide (Johnston et al., 2012), but not definitively demonstrated. A large enrichment of ^{57}Fe in lepidocrocite would have the effect of diluting the Mössbauer signals from the other phases, including the goethite, and may explain the difference between the measured and reconstructed Mössbauer spectra from reactors containing unsubstituted jarosite.

4.4. Implications

The rapid transformation of jarosite in this study was consistent with the observed absence of jarosite in acid sulfate topsoils (Grigg et al.,

2024; Van Breemen and Harmsen, 1975). In terms of Fe(II) concentration (Burton et al., 2011; Karimian et al., 2017) and pH (Kölbl et al., 2017), the solution in the reactors was analogous to pore water from some flooded acid sulfate topsoils. Therefore, the rate and pathways of jarosite transformation in this study may be relevant to understand the processes that drive jarosite transformation in the upper horizons of ASS or in ASS horizons that are amended to promote reducing conditions. Additionally, the results could be used to interpret the transformation of jarosite additions to soil if the soils are amended to raise their pH, or the transformation of jarosite from AMD during flows into less acidic waterways. The outcomes of Fe(II)-catalysed jarosite recrystallisation, and balance between hydrolysis and Fe(II)-catalysed jarosite transformation, could be significant to interpret jarosite dynamics in redox-active soils. In particular, the abundance of lepidocrocite among the products of jarosite transformation, the role of lepidocrocite as a sink for metal ions, and the formation of lepidocrocite during jarosite hydrolysis in the presence of Fe(II) are phenomena that have not been previously considered in the context of jarosite transformation. Lepidocrocite may be a more stable phase than ferrihydrite in soil, and has unique transformation behaviour in soils that are regularly flooded and drained (Schulz et al., 2023).

Transformation of jarosite in the field may be dependent not only on the soil conditions, but also on the characteristics of the jarosite particles and crystal structure (Gasharova et al., 2005). The results of this study provide insights into the important role that one factor, Al-for-Fe substitution, plays in regulating the rates and pathways of jarosite transformation. In synthetic samples, Al-for-Fe substitution slowed jarosite transformation and promoted the formation of goethite and ferrihydrite over lepidocrocite. Although Fe(II) increased the rate of jarosite transformation by a factor of 80 % to 750 % above the rate of transformation due to hydrolysis at circumneutral pH, the effect of 7 % Al substitution on the transformation rate was larger than a one-order-of-magnitude difference in the Fe(II) concentration. The effect of Al was most strongly observed in Fe(II)-catalysed transformations, whereas Al has a lesser effect on the rate of jarosite hydrolysis.

The effects of element substitution other than Al-for-Fe substitution, and the effects of crystal morphology, were further illustrated by the slow rate of natural jarosite transformation in comparison to the synthetic jarosite, and different patterns of secondary mineral growth on the natural jarosite particles. Understanding the role of ion substitution and mineral morphology on stability under field conditions is critical to predicting the impact of jarosite on the biogeochemistry of acid sulfate environments, such as ASS, during its geochemical evolution. Aluminium-for-Fe substitution should be considered as an important factor leading to the stabilisation of jarosite in acid sulfate environments.

Data availability

Associated research data for plots presented in this manuscript are available from the ETH Research Collection at https://doi.org/10.3929/ethz-b-000636002.

CRediT authorship contribution statement

Andrew R.C. Grigg: Conceptualization, Methodology, Investigation, Formal analysis, Visualization, Writing – original draft. **Luiza Notini:** Writing – review & editing, Methodology. **Ralf Kaegi:** Writing – review & editing, Investigation. **Laurel K. ThomasArrigo:** Conceptualization, Methodology, Supervision, Writing – review & editing. **Ruben Kretzschmar:** Writing – review & editing, Supervision, Project administration, Methodology, Funding acquisition, Conceptualization.

Declaration of competing interest

The authors declare that they have no known competing financial interests or personal relationships that could have appeared to influence the work reported in this paper.

Acknowledgments

The authors gratefully acknowledge Kurt Barmettler, Katherine Rothwell and Giulia Fantappiè (ETH Zurich) for assistance in the laboratory. We wish to thank Worachart Wisawapipat (Kasetsart University, Bangkok), Katrin Schulz and Kurt Barmettler (ETH Zurich) for assistance with field work in Thailand. Fieldwork in Thailand was approved by the Office of the National Research Council of Thailand (no. 0002/1164). This research is part of a project that has received funding from the European Research Council (ERC) under the European Union's Horizon 2020 research and innovation programme (788009-IRMIDYN-ERC-2017-ADG).

Appendix A. Supplementary material

The supplementary material contains additional results and explanations on the topics: (S1) jarosite characterisation, (S2) solution composition measurements, (S3) additional electron microscopy and EDX element mapping, (S4) data extracted from the Rietveld fitting of X-ray diffraction patterns, (S5) data extracted from Raman spectroscopy, (S6) analysis of Mössbauer spectroscopy, (S7) detailed methodology and results of the atom-flow modelling, and (S8) plotted XRD patterns, plotted Raman spectra, tabulated data extracted from Rietveld fitting of X-ray diffraction and python code for the atom-flow model. Supplementary material to this article can be found online at https://doi.org/10.1016/j.gca.2024.04.008.

References

Aeppli, M., Kaegi, R., Kretzschmar, R., Voegelin, A., Hofstetter, T.B., Sander, M., 2019. Electrochemical analysis of changes in iron oxide reducibility during abiotic ferrihydrite transformation into goethite and magnetite. Environ. Sci. Technol. 53, 3568–3578.

Alpers, C.N., Rye, R.O., Nordstrom, D.K., White, D.L., King, B.-S., 1992. Chemical, crystallographic and stable isotopic properties of alunite and jarosite from acid-hypersaline Australian lakes. Chem. Geol. 96, 203–226.

Baccolo, G., Delmonte, B., Niles, P.B., Cibin, G., Di Stafano, E., Hampai, D., Keller, L., Maggi, V., Marcelli, A., Michalski, J., Snead, C., Frezzotti, M., 2021. Jarosite formation in deep Antarctic ice provides a window into acidic, water-limited weathering on Mars. Nat. Commun. 12, 436.

Bigham, J.M., Nordstrom, D.K., 2000. Iron and aluminum hydroxysulfates from acid sulfate waters. Rev. Mineral. Geochem. 40, 351–403.

Burton, E.D., Bush, R.T., Johnston, S.G., Sullivan, L.A., Keene, A.F., 2011. Sulfur biogeochemical cycling and novel Fe-S mineralization pathways in a tidally re-flooded wetland. Geochim. Cosmochim. Acta 75, 3434–3451.

Carson, C.D., Fanning, D.S., Dixon, J.B., 1982. Alfisols and ultisols with acid sulfate weathering features in Texas. In: Kittrick, J.A., Fanning, D.S., Hossner, L.R. (Eds.), Acid Sulfate Weathering. Soil Science Society of America, Madison, WI USA.

Chen, K., Jin, X., Guo, C., He, C., Zhang, Y., Gao, K., Lu, G., Dang, Z., 2021. Reductive dissolution of Pb-Zn jarosite under near-neutral conditions. Chem. Geol. 579, 120338.

Driscoll, R.L., Leinz, R.W., 2005. Method for Synthesis of Some Jarosites, Techniques and Methods 5-D. U.S. Geological Survey.

Driscoll, C.T., Schecher, W.D., 1990. The chemistry of aluminium in the environment. Environ. Geochem. Health 12, 28–49.

Dutrizac, J.E., Jambor, J.L., 2000. Jarosites and their application in hydrometallurgy. Rev. Mineral. Geochem. 40, 405–452.

Fanning, D.S., 1993. Salinity problems in acid sulfate coastal soils. In: Lieth, H., Al Masoom, A. (Eds.), Towards the Rational Use of High Salinity Tolerant Plants. Kluwer Academic Publishers, pp. 491–500.

Fleet, M.E., 1981. The structure of magnetite. Acta Cryst. Sect. B B37, 917–920.

Frierdich, A.J., Scherer, M.M., Bachman, J.E., Engelhard, M.H., Rapponotti, B.W., Catalano, J.G., 2012. Inhibition of trace element release during Fe(II)-activated recrystallization of Al-, Cr- and Sn-substituted goethite and hematite. Environ. Sci. Technol. 46, 10031–10039.

Gasharova, B., Göttlicher, J., Becker, U., 2005. Dissolution at the surface of jarosite: an in situ AFM study. Chem. Geol. 215, 499–516.

Gorski, C.A., Scherer, M.M., 2011. Fe2+ sorption at the Fe oxide-water interface: a revised conceptual framework. In: Tratnyek, P.G., Grundl, T.J., Haderlein, S.B. (Eds.), Aquatic Redox Chemistry. American Chemical Society, Washington, DC, USA, pp. 315–343.

Grigg, A.R.C., ThomasArrigo, L.K., Schulz, K., Rothwell, K.A., Kaegi, R., Kretzschmar, R., 2022. Ferrihydrite transformations in flooded paddy soils: rates, pathways, and product spatial distributions. Environ. Sci.: Process. Impacts 24, 1867–1882.
Grigg, A.R.C., Notini, L., Kaegi, R., ThomasArrigo, L.K., Kretzschmar, R., 2024. Structural effects of aluminum and iron occupancy in minerals of the jarosite-alunite solid solution. ACS Earth Space Chem. 8, 194–206.
Hansel, C.M., Benner, S.G., Fendorf, S., 2005. Competing Fe(II)-induced mineralization pathways of ferrihydrite. Environ. Sci. Technol. 39, 7147–7153.
Hansel, C.M., Learman, D.R., Lentini, C.J., Ekstrom, E.B., 2011. Effect of adsorbed and substituted Al on Fe(II)-induced mineralization pathways of ferrihydrite. Geochim. Cosmochim. Acta 75, 4653–4666.
Johnston, J.H., 1977. Jarosite and akaganéite from White Island volcano, New Zealand: an X-ray and Mössbauer study. Geochim. Cosmochim. Acta 41, 539–544.
Johnston, S.G., Burton, E.D., Keene, A.F., Planer-Friedrich, B., Voegelin, A., Blackford, M. G., Lumpkin, G.R., 2012. Arsenic mobilization and iron transformations during sulfidization of As(V)-bearing jarosite. Chem. Geol. 334, 9–24.
Jones, F., 2017. Crystallization of jarosite with variable Al^{3+} content: the transition to alunite. Minerals 7, 90.
Jones, A.M., Collins, R.N., Rose, J., Waite, T.D., 2009. The effect of silica and natural organic matter on the Fe(II)-catalysed transformation and reactivity of Fe(III) minerals. Geochim. Cosmochim. Acta 73, 4409–4422.
Joshi, P., Fantle, M.S., Boualavong, J., Gorski, C.A., 2022. Quantifying the rate of Fe^{2+}-catalyzed recrystallization based on a unifying model framework. Geochim. Cosmochim. Acta 336, 423–435.
Karimian, N., Johnston, S.G., Burton, E.D., 2017. Antimony and arsenic behaviour during Fe(II)-induced transformation of jarosite. Environ. Sci. Technol. 51, 4259–4268.
Karimian, N., Johnston, S.G., Burton, E.D., 2018. Antimony and arsenic partitioning during Fe^{2+}-induced transformation of jarosite under acidic conditions. Chemosphere 195, 515–523.
Kendall, M.R., Madden, A.S., Elwood Madden, M.E., Hu, Q., 2013. Effects of arsenic incorporation on jarosite dissolution rate and reaction products. Geochim. Cosmochim. Acta 112, 192–207.
Klingelhöfer, G., Morris, R.V., Bernhardt, B., Schroöder, C., Rodionov, D.S., de Souza, P. A., Yen, A., Gellert, R., Evlanov, N., Zubkov, B., Foh, J., Bonnes, U., Kankeleit, E., Gütlich, P., Ming, D.W., Renz, F., Wdowiak, T., Squyres, S.W., Arvidson, R.E., 2004. Jarosite and hematite at Meridiani Planum from Opportunity's Mössbauer spectrometer. Science 306, 1740–1745.
Kölbl, A., Marschner, P., Fitzpatrick, R., Mosley, L., Kögel-Knabner, I., 2017. Linking organic matter composition in acid sulfate soils to pH recovery after re-submerging. Geoderma 308, 350–362.
Lagarec, K., Rancourt, D.G., 1997. Extended Voigt-based analytic lineshape method for determining N-dimensional correlated hyperfine parameter distributions in Mössbauer spectroscopy. Nucl. Instrum. Methods in Phys. Res. B 129, 266–280.
Larese-Casanova, P., Haderlein, S.B., Kappler, A., 2010. Biomineralization of lepidocrocite and goethite by nitrate-reducing Fe(II)-oxidizing bacteria: effect of pH, bicarbonate, phosphate, and humic acids. Geochim. Cosmochim. Acta 74, 3721–3734.
Latta, D.E., Bachman, J.E., Scherer, M.M., 2012. Fe electron transfer and atom exchange in goethite: influence of Al-substitution and anion sorption. Environ. Sci. Technol. 46, 10614–10623.
Liao, S., Wang, X., Yin, H., Post, J.E., Yan, Y., Tan, W., Huang, Q., Liu, F., Feng, X., 2020. Effects of Al substitution on local structure and morphology of lepidocrocite and its phosphate adsorption kinetics. Geochim. Cosmochim. Acta 276, 109–121.
Liu, H., Chen, T., Zou, X., Qing, C., Frost, R.L., 2013. Effect of Al content on the structure of Al-substituted goethite: a micro-Raman spectroscopic study. J. Raman Spectrosc. 44, 1609–1614.
Ljung, K., Maley, F., Cook, A., Weinstein, P., 2009. Acid sulfate soils and human health—a Millennium Ecosystem Assessment. Environ. Int. 35, 1234–1242.
Masue-Slowey, Y., Loeppert, R.H., Fendorf, S., 2011. Alteration of ferrihydrite reductive dissolution and transformation by adsorbed As and structural Al: implications for As retention. Geochim. Cosmochim. Acta 75, 870–886.
Mees, F., Stoops, G., 2018. Sulphidic and sulphuric materials. In: Stoops, G., Marcelino, V., Mees, F. (Eds.), Interpretation of Micromorphological Features of Soils and Regoliths, 2e. Elsevier B.V.
Menchetti, S., Sabelli, C., 1976. Crystal chemistry of the alunite series: crystal structure refinement of alunite and synthetic jarosite. Neues Jahrb. für Mineral. Monatshefte 9, 406–417.
Miller, J.L., Elwood Madden, A.S., Phillips-Lander, C.M., Pritchett, B.N., Elwood Madden, M.E., 2016. Alunite dissolution rates: dissolution mechanisms and implications for Mars. Geochim. Cosmochim. Acta 172, 93–106.
Notini, L., ThomasArrigo, L.K., Kaegi, R., Kretzschmar, R., 2022. Coexisting goethite promotes Fe(II)-catalyzed transformation of ferrihydrite to goethite. Environ. Sci. Technol. 56, 12723–12733.
Pappu, A., Saxena, M., Asolekar, S.R., 2006. Jarosite characteristics and its utilisation potentials. Sci. Total Environ. 359, 232–243.
Pedersen, H.D., Postma, D., Jakobsen, R., Larsen, O., 2005. Fast transformation of iron oxyhydroxides by the catalytic action of aqueous Fe(II). Geochim. Cosmochim. Acta 69, 3967–3977.
Poulton, S.W., Krom, M.D., Raiswell, R., 2004. A revised scheme for the reactivity of iron (oxyhydr)oxide minerals towards dissolved sulfide. Geochim. Cosmochim. Acta 68, 3703–3715.
Powell, B., Martens, M., 2005. A review of acid sulfate soil impacts, actions and policies that impact on water quality in Great Barrier Reef catchments, including a case study on remediation at East Trinity. Mar. Pollut. Bull. 51, 149–164.
Rancourt, D.G., Ping, J.-Y., 1991. Voigt-based methods for arbitrary-shape static hyperfine parameter distributions in Mössbauer spectroscopy. Nucl. Instrum. Methods in Phys. Res. B 58, 85–97.
Renishaw plc, 2018. Renishaw Technical Note no. TN214(EN)-01-A. Technical note: LiveTrack focus-tracking technology. https://resources.renishaw.com/download.aspx?lang=en&data=103910&btn=1 (accessed 21 January 2022).
Ryu, J.-G., Kim, Y., 2022. Mineral transformation and dissolution of jarosite coprecipitated with hazardous oxyanions and their mobility changes. J. Hazard. Mater. 427, 128283.
Sánchez-España, J., Yusta, I., Gray, J., Burgos, W.D., 2016. Geochemistry of dissolved aluminium at low pH: extent and significnace of Al-Fe(III) coprecipitation below pH 4.0. Geochim. Cosmochim. Acta 175, 128–149.
Scarlett, N.V.Y., Madsen, I.C., 2006. Quantification of phases with partial or no known crystal structures. Powder Diffr. 21, 278–284.
Schulz, K., ThomasArrigo, L.K., Kaegi, R., Kretzschmar, R., 2022. Stabilization of ferrihydrite and lepidocrocite by silicate during Fe(II)-catalyzed mineral transformation: impact on particle morphology and silicate distribution. Environ. Sci. Technol. 56, 5929–5938.
Schulz, K., Notini, L., Grigg, A.R.C., Kubeneck, L.J., Wisawapipat, W., ThomasArrigo, L. K., Kretzschmar, R., 2023. Contact with soil impacts ferrihydrite and lepidocrocite transformations during redox cycling in a paddy soil. Environ. Sci.: Process. Impacts 53, 1945–1961.
Schulze, D.G., 1984. The influence of aluminium on iron oxides. VIII. Unit-cell dimensions of Al-substituted goethites and estimation of Al from them. Clays Clay Miner. 32, 36–44.
Schwertmann, U., Wolska, E., 1990. The influence of aluminum on iron oxides. XV. Al-for-Fe substitution in synthetic lepidocrocite. Clays Clay Miner. 38, 209–212.
Sheng, A., Liu, J., Li, X., Qafoku, O., Collins, R.N., Jones, A.M., Pearce, C.I., Wang, C., Ni, J., Lu, A., Rosso, K.M., 2020. Labile Fe(III) from sorbed Fe(II) oxidation is the key intermediate in Fe(II)-catalyzed ferrihydrite transformation. Geochim. Cosmochim. Acta 272, 105–120.
Smith, A.M.L., Hudson-Edwards, K.A., Dubbin, W.E., Wright, K., 2006. Dissolution of jarosite $[KFe_3(SO_4)_2(OH)_6]$ at pH 2 and 8: insights from batch experiments and computational modelling. Geochim. Cosmochim. Acta 70, 608–621.
Stoffregen, R.E., Alpers, C.N., Jambor, J.L., 2000. Alunite-jarosite crystallography, thermodynamics and geochronology. Rev. Mineral. Geochem. 40, 454–479.
Taylor, P.D.P., Maeck, R., De Bièvre, P., 1992. Determination of the absolute isotopic composition and atomic weight of a reference sample of natural iron. Int. J. Mass Spectrom. 121, 111–125.
Taylor, R.M., Schwertmann, U., 1978. The influence of aluminium on iron oxides. Part I. The influence of Al on Fe oxide formation from the Fe(II) system. Clays Clay Miner. 26, 373–383.
ThomasArrigo, L.K., Byrne, J., Kappler, A., Kretzschmar, R., 2018. Impact of organic matter on iron(II)-catalyzed mineral transformations in ferrihydrite-organic matter coprecipitates. Environ. Sci. Technol. 52, 12316–12326.
ThomasArrigo, L.K., Kaegi, R., Kretzschmar, R., 2019. Ferrihydrite growth and transformation in the presence of ferrous iron and model organic ligands. Environ. Sci. Technol. 53, 13636–13647.
Van Breemen, N., 1973. Dissolved aluminum in acid sulfate soils and in acid mine waters. Soil Sci. Soc. Am. J. 37, 694–697.
Van Breemen, N., Harmsen, K., 1975. Translocation of iron in acid sulfate soils: I. Soil morphology, and the chemistry and mineralogy of iron in a chronosequence of acid sulfate soils. Soil Sci. Soc. Am. J. 39, 1140.
Wan, M., Schröder, C., Peiffer, S., 2017. Fe(III):S(-II) concentration ratio controls the pathway and the kinetics of pyrite formation during sulfidation of ferric hydroxides. Geochim. Cosmochim. Acta 217, 334–348.
Welch, S.A., Christy, A.G., Kirste, D., Beavis, S.G., Beavis, F.R., 2007. Jarosite dissolution I - Trace cation flux in acid sulfate soils. Chem. Geol. 245, 183–197.
Welch, S.A., Kirste, D., Christy, A.G., Beavis, F.R., Beavis, S.G., 2008. Jarosite dissolution II - reaction kinetics, stoichiometry and acid flux. Chem. Geol. 254, 73–86.
Whitworth, A.J., Brand, H.E.A., Frierdich, A.J., 2020. Iron isotope exchange and fractionation between jarosite and aqueous Fe(II). Chem. Geol. 554, 119802.
Williams, A.G.B., Scherer, M.M., 2004. Spectroscopic evidence for Fe(II)-Fe(III) electron transfer at the iron oxide-water interface. Environ. Sci. Technol. 38, 4782–4790.
Yvanes-Giuliani, Y.A.M., Waite, T.D., Collins, R.N., 2014. Exchangeable and secondary mineral reactive pools of aluminium in coastal lowland acid sulfate soils. Sci. Total Environ. 485–486, 232–240.
Zepeda-Alarcon, E., Nakotte, H., Gualtieri, A.F., King, G., Page, K., Vogel, S.C., Wang, H.-W., Wenk, H.-R., 2014. Magnetic and nuclear structure of goethite (α-FeOOH): a neutron diffraction study. J. Appl. Crystallogr. 47.
Zhukhlistov, A.P., 2001. Crystal structure of lepidocrocite FeO(OH) from electron diffraction data. Kristallografiya 46.